

# Double-impulse magnetic focusing of launched cold atoms

Aidan S Arnold<sup>†</sup>, Matthew J Pritchard<sup>‡</sup>, David A Smith<sup>‡</sup> and Ifan G Hughes<sup>‡</sup>

<sup>†</sup> Department of Physics, University of Strathclyde, Glasgow, G4 0NG, UK

<sup>‡</sup> Department of Physics, Rochester Building, University of Durham, South Road, Durham, DH1 3LE, UK

E-mail: i.g.hughes@durham.ac.uk

**Abstract.** We have theoretically investigated 3D focusing of a launched cloud of cold atoms using a pair of magnetic lens pulses (the alternate-gradient method). Individual lenses focus radially and defocus axially or vice-versa. The performance of the two possible pulse sequences are compared and found to be ideal for loading both ‘pancake’ and ‘sausage’ shaped magnetic/optical microtraps. It is shown that focusing aberrations are considerably smaller for double-impulse magnetic lenses compared to single-impulse magnetic lenses. An analysis of the clouds focused by double-impulse technique is presented.

PACS numbers: 32.80.Pj, 42.50.Vk

## 1. Introduction

The field of atom optics [1] has undergone a dramatic expansion in the last two decades, largely as a consequence of the development of laser-cooling techniques [2], and the routine production of atoms at microKelvin temperatures [3]. Paramagnetic cold atoms can be manipulated with the Stern-Gerlach force [4]. To date, the Stern-Gerlach force has been used to realise a variety of atomic mirrors for both cold [5] and Bose condensed atoms [6]. This paper, however, concentrates on the formation of magnetic lenses for cold atoms. In comparison to a ballistically expanding unfocused cloud, a magnetically focused cloud can lead to density increases (or conversely temperature decreases) of many orders of magnitude. Applications include: atom lithography [7]; transferring cold atoms from a Magneto Optical Trap (MOT) to a remote vacuum chamber of lower background pressure [8]; cold low-density atomic sources for fountain clocks [9].

The first demonstration of 3D focusing with pulsed magnetic lenses was conducted by Cornell *et al.* [10]. The group of Gorceix have made experimental and theoretical studies of cold atom imaging by means of pulsed magnetic fields [11, 12]. However, neither work addressed the optimum strategy for achieving a compact focused cloud, nor the limiting features for the quality of their atom-optical elements.

Recently we provided a theoretical analysis of 3D focusing of weak-field-seeking cold atoms using a single magnetic pulse [13]. Lens designs for 1D and 3D were presented that minimise aberrations due to the lens potential’s departure from the

perfect parabolic case. Single-impulse 3D focusing has been experimentally achieved at Durham University, the results of which can be seen in a forthcoming publication [14].

The scope of this paper is to investigate theoretically and numerically the limiting factors to the quality and size of the final image obtained in double-impulse magnetic focusing experiments; to identify the sources of aberration; and to discuss schemes for minimising their effect. We will show that both single- and double-impulse lenses yield a magnetically focused cloud with a bimodal distribution consisting of a highly diffuse outer cloud, as well as a core cloud which can be orders of magnitude denser than the initial atomic sample. This core cloud is therefore ideal for remotely loading tight traps with relatively small depth, e.g. miniature magnetic guides [15], atom chips [4, 16] and optical dipole traps [17].

The remainder of the paper is organised as follows: Section 2 outlines the theory of how to achieve the desired magnetic fields; Section 3 contains an analysis of magnetic imaging and minimising the final cloud size; Section 4 describes and contrasts the spatial performance of different magnetic lenses; Section 5 considers experimentally relevant parameters for alternate gradient lenses; Section 6 contains a discussion and concluding remarks.

## 2. Alternate-gradient lens theory

An atom in a magnetic field of magnitude  $B$  experiences a magnetic dipole interaction energy of  $U = -\mu_\zeta B$ , where  $\mu_\zeta$  is the projection of the atom's magnetic moment onto the field direction. Provided that Majorana spin-flip transitions [18] occurring in field zeros are avoided and the rate of change of direction of the field is less than the Larmor frequency the magnetic moment adiabatically follows the field.

The Stern-Gerlach force is  $\vec{F}_{\text{SG}} = -\nabla U = \nabla(\mu_\zeta B)$ . The ensemble (of alkali metal atoms) can be optically pumped into either a strong-field-seeking state with  $\mu_\zeta = \mu_B$  (where  $\mu_B$  is the Bohr magneton), or into a weak-field-seeking state with  $\mu_\zeta = -\mu_B$ . In low field, where the quantum numbers  $F$  and  $m_F$  are good, these states are the stretched states  $|F = I + 1/2, m_F = \pm F\rangle$ . Atoms in these states have a magnetic moment which is independent of field, consequently the Stern-Gerlach force takes the simpler form  $\vec{F}_{\text{SG}} = \pm\mu_B\nabla B$  — i.e. the focusing of the atoms is governed by the gradient of the magnetic field magnitude only.

The choice of whether atoms in weak or strong-field seeking states are launched depends on the particular application. We discussed extensively in [13] the focusing of atoms in weak-field-seeking states. This was because single-impulse 3D imaging of strong-field-seeking states requires a maximum of the magnetic field in free space, which is forbidden by Earnshaw's theorem [19].

In this paper magnetic lenses centred on the point  $\{0, 0, z_c\}$  are considered, with a second order magnetic field magnitude of the form:

$$B(x, y, z) = B_0 + \frac{B_2}{2} (-x^2/2 - y^2/2 + (z - z_c)^2). \quad (1)$$

$B_0$  and  $B_2$  are the bias field and the field curvature, respectively. Substituting this into the Stern-Gerlach force expression results in an atom of mass  $m$  experiencing a harmonic acceleration about  $\{0, 0, z_c\}$ :

$$\mathbf{a} = -\omega^2 \{-x/2, -y/2, (z - z_c)\}, \quad (2)$$

where  $\omega^2 = \mu_\zeta B_2/m$  is a measure of the power of the lens. The axial curvature is twice the magnitude of, and opposite in sign to, the radial curvature,  $\omega_z^2 = -2\omega_r^2$ .

Note that lens curvature in all three spatial dimensions is reversed if the sign of either  $\mu_\zeta$  or  $B_2$  is reversed. For simplicity from this point on, only the case  $\mu_\zeta = -\mu_B$  i.e. weak-field-seeking atoms will be used and lens curvature is modified solely via  $B_2$ .

We refer to a lens with a field expansion of the form  $B$  as a one-dimensional lens, as it can be used either to focus axially (with simultaneous radial defocusing), when  $B_2$  is positive, or to focus radially (with simultaneous axial defocusing) when  $B_2$  is negative. In order to achieve a 3D focus with the lenses of equation (2), an axially converging lens pulse must be followed by an appropriately timed axially diverging lens (or vice versa). This is referred to as the ‘‘alternate gradient’’ focusing method, and has the advantage of being able to focus both weak-field and strong-field seeking atoms. This method is used extensively in particle accelerators [20], for focusing polar molecules [21], and is shown schematically in Figure 1. Useful parameters for describing the evolution of a Gaussian atomic cloud are the axial ( $\sigma_z$ ) and radial ( $\sigma_r$ ) rms cloud radii (the standard deviations), as well as their aspect ratio  $\xi = \sigma_z/\sigma_r$ .

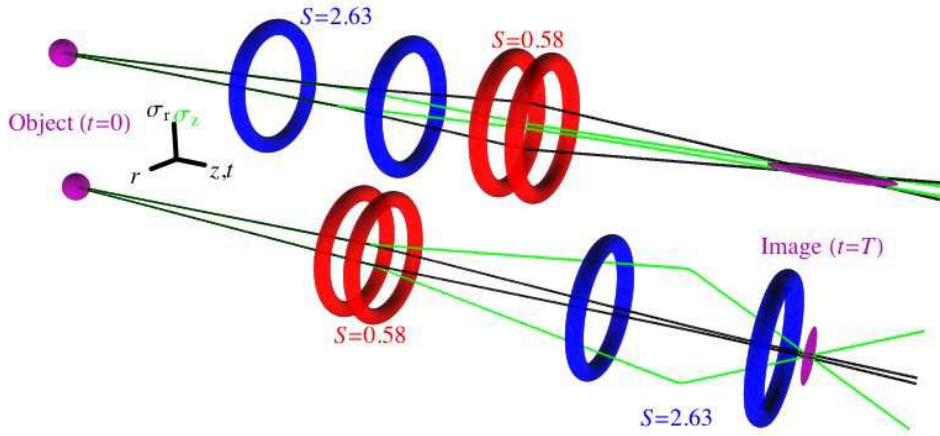


**Figure 1.** The principle of alternate gradient focusing. The upper image, Strategy AR, shows the evolution of the axial ( $\sigma_z$ , green) and radial ( $\sigma_r$ , black) cloud radii when an axially converging (radially diverging) lens precedes an axially diverging (radially converging) lens and leads to a sausage-shaped cloud ( $\xi > 1$ ). In the lower image, Strategy RA, the lens order is reversed, leading to a pancake-shaped cloud ( $\xi < 1$ ). The effects of gravity (in the  $-z$  direction along the coil axis) are not shown, but are included in simulations. Due to the time reversal symmetry of optics, the lens system also works backwards.

As shown in reference [13] there exist optimal configurations for realising radial and axial focusing lenses. These are achieved with a pair of separated coaxial coils, where both coils have equal current with the same sense. An important lens parameter is the relative separation  $S$  of the coils in units of the coil radius. The harmonicity of a radially-focusing lens is optimized if  $S = 0.58$  (red lenses in Figure 1); whereas the harmonicity of an axially-focusing lens is optimized if  $S = 2.63$  (blue lenses in Figure 1). In the remainder of this work it is assumed that these optimized lenses are used.

### 3. Magnetic impulses and the ABCD formalism

The separable equations of motion for an axially and cylindrically symmetric coil system lead to a lens that is harmonic in 3D with an acceleration given by equation (2), which allows the motion in each cartesian dimension to be treated as a separate simple harmonic equation. The influence of a magnetic lens can be described by  $ABCD$  matrices, as outlined in [12, 13]. The initial and final position and velocity of an atom along a given Cartesian axis, say  $x$ , are related via the equation:

$$\begin{pmatrix} x_f \\ v_{x_f} \end{pmatrix} = \begin{pmatrix} \mathcal{A} & \mathcal{B} \\ \mathcal{C} & \mathcal{D} \end{pmatrix} \begin{pmatrix} x_i \\ v_{x_i} \end{pmatrix}. \quad (3)$$

A ‘thick’ converging lens of strength  $\omega$  (with  $\text{Im}(\omega) = 0$ ) and physical duration  $\tau$  is actually equivalent to the ‘thin’ lens  $ABCD$  transformation:

$$\begin{pmatrix} \cos(\omega\tau) & \frac{1}{\omega} \sin(\omega\tau) \\ -\omega \sin(\omega\tau) & \cos(\omega\tau) \end{pmatrix} = \begin{pmatrix} 1 & \tau'/2 \\ 0 & 1 \end{pmatrix} \begin{pmatrix} 1 & 0 \\ \mathcal{C} & 1 \end{pmatrix} \begin{pmatrix} 1 & \tau'/2 \\ 0 & 1 \end{pmatrix}, \quad (4)$$

where  $\mathcal{C}(\omega, \tau) = -\omega \sin(\omega\tau)$ , and is pre- and post-multiplied by a translation matrix of half the effective pulse width  $\tau'(\omega, \tau) = \frac{2}{\omega} \tan(\frac{\omega\tau}{2})$ . The notation of primes is used to denote times in the ‘thin’ lens representation. To model a diverging lens make the transformation  $\omega \rightarrow \pm i\omega$  in equation (4) – i.e.  $\mathcal{C} = \omega \sinh(\omega\tau)$  and  $\tau' = \frac{2}{\omega} \tanh \frac{\omega\tau}{2}$ . The ‘equivalent time’ of the lens  $\tau'$  is not the same as the real experimental pulse duration of  $\tau$ .

#### 3.1. Double impulse magnetic lenses - the parabolic case

A double lens system, see Figure 2, comprising lenses of strength and duration  $\omega_1, \tau_1$  (starting after a time  $t_1$ ) and  $\omega_2, \tau_2$  (starting a time  $t_2$  after the first lens) is modelled by using the following  $ABCD$  matrix sequence:

$$\begin{pmatrix} \mathcal{A} & \mathcal{B} \\ \mathcal{C} & \mathcal{D} \end{pmatrix} = \begin{pmatrix} 1 & t'_3 \\ 0 & 1 \end{pmatrix} \begin{pmatrix} 1 & 0 \\ \mathcal{C}_2 & 1 \end{pmatrix} \begin{pmatrix} 1 & t'_2 \\ 0 & 1 \end{pmatrix} \begin{pmatrix} 1 & 0 \\ \mathcal{C}_1 & 1 \end{pmatrix} \begin{pmatrix} 1 & t'_1 \\ 0 & 1 \end{pmatrix}, \quad (5)$$

i.e. a  $t'_1 = t_1 + \frac{1}{2}\tau'_1$  translation, then a strength  $\mathcal{C}_1$  thin lens, a  $t'_2 = \frac{1}{2}\tau'_1 + t_2 + \frac{1}{2}\tau'_2$  translation, then a strength  $\mathcal{C}_2$  thin lens followed by a  $t'_3 = T' - t'_1 - t'_2$  translation, where  $\mathcal{C}_j = -\omega_j \sin(\omega_j \tau_j)$  and  $\tau'_j = \frac{2}{\omega_j} \tan(\frac{\omega_j \tau_j}{2})$  for  $j \in \{1, 2\}$ . The total physical duration of the focusing,  $T$ , is fixed, and the effective total time of the double lens system is  $T' = T - \tau_1 - \tau_2 + \tau'_1 + \tau'_2$ .

By multiplying the matrices of equation (5) together, the final  $ABCD$  system matrix is obtained. An image (i.e. a one-to-one map of position between the initial and final cloud) is formed if the condition  $\mathcal{B} = 0$  is maintained. In this case the spatial magnification  $\mathcal{A}$  is the inverse of the velocity magnification  $\mathcal{D}$ ; a manifestation of Liouville’s theorem. The cloud extent along  $x$  in a given plane is given by:

$$\sigma_{x_f}^2 = (\mathcal{A}\sigma_{x_i})^2 + (\mathcal{B}\sigma_{v_{x_i}})^2, \quad (6)$$

where  $\sigma_{x_i}$  is the initial position standard deviation and  $\sigma_{v_{x_i}}$  is the initial velocity standard deviation. An *image* is formed for the condition  $\mathcal{B} = 0$ , but the *smallest cloud size* occurs when one minimises the product of the cloud extent for all 3 spatial dimensions (i.e.  $\sigma_{r_f}^2 \sigma_{z_f}$ ). For single- and double-impulse lens systems, the cloud size at the image plane and the minimum cloud size do not correspond exactly, but they are usually very similar. In the rest of the paper we will consider the cloud size at the image plane ( $\mathcal{B} = 0$ ), and thus  $\mathcal{A}$  corresponds to the magnification.

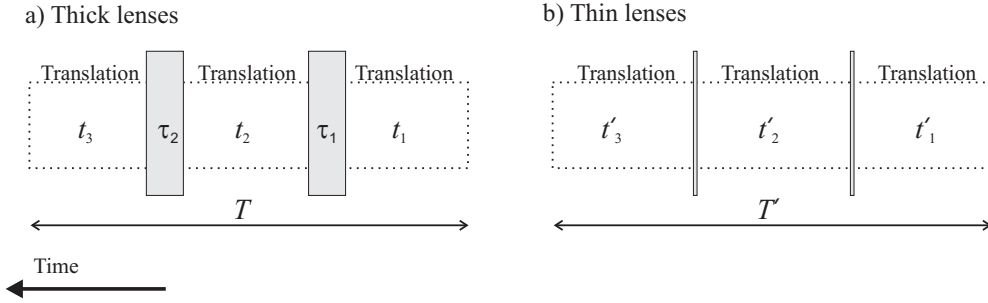


**Figure 2.** A schematic diagram showing the timing sequences for the two frames of reference. (a) shows the thick lens or lab frame with the time durations for each stage and (b) shows the mathematically equivalent thin lens representation that is used in the calculations. Note that the direction of time runs right to left so that it visually mirrors the system matrix layout in equation (5).

### 3.2. Solving the matrix equations

The important entries of the system matrix in equation (5) are  $\mathcal{A}$  and  $\mathcal{B}$ :

$$\mathcal{A} = 1 + (\mathcal{C}_1 + \mathcal{C}_2)(T' - t'_1) + \mathcal{C}_2(-1 + \mathcal{C}_1(T' - t'_1))t'_2 - \mathcal{C}_1\mathcal{C}_2t'^2_2 \quad (7)$$

$$\mathcal{B} = T' + \mathcal{C}_2(T' - t'_1 - t'_2)(t'_1 + t'_2) + \mathcal{C}_1t'_1(T' + \mathcal{C}_2(T' - t'_2)t'_2 - t'_1(1 + \mathcal{C}_2t'_2)), \quad (8)$$

which are both second order in  $t'_1$  and  $t'_2$  (and hence also second order in  $t_1$  and  $t_2$ ).

To obtain an atom cloud which is focused in all 3 dimensions requires that the first lens is axially converging (radially diverging) and the second lens is axially diverging (radially converging), or vice versa. Moreover, the radial (subscript  $r$ ) and axial (subscript  $z$ ) spatial dimensions have different  $\mathcal{A}$  and  $\mathcal{B}$  coefficients. If the two axial lens strengths are  $\omega_{1z}$  and  $\omega_{2z}$ , then equation (2) yields  $\omega_{1r} = i\omega_{1z}/\sqrt{2}$  and  $\omega_{2r} = i\omega_{2z}/\sqrt{2}$ . A 3D image is formed when equation (8) is set equal to zero for both the radial and axial directions.

In reference [13] the density increase from a single-impulse isotropic 3D harmonic lens,  $\lambda^3/(1 - \lambda)^3$ , was characterised by  $\lambda$ , the equivalent time of the thin lens,  $t'_1$ , relative to the total equivalent focus time  $T'$ . Note that for the anisotropic lenses in this paper the *equivalent* (i.e. thin lens) timing of a lens in the radial and axial direction is different. For this reason we will characterise alternate-gradient lensing with the parameters  $\{\lambda_1, \lambda_2\} = \{t_1 + \tau_1/2, t_1 + \tau_1 + t_2 + \tau_2/2\}/T$ , corresponding to the mean times of the first and second magnetic impulses relative to the total experimental lensing time  $T$ . We use this labelling of  $\{\lambda_1, \lambda_2\}$  if  $\omega_{1r}$  is real (the first lens is radially converging), and we swap the definitions of  $\lambda_1$  and  $\lambda_2$  if  $\omega_{1r}$  is imaginary (the first lens is radially diverging).

Modelling an experiment being conducted at Durham University [14], we fix  $T = 212$  ms. The cold atom cloud has an isotropic initial spatial and velocity distribution with 1D standard deviations of  $\sigma_R = 0.4$  mm and  $\sigma_V = 4.4$  cm/s (i.e. a temperature of  $20 \mu\text{K}$ ) respectively. The coils are assumed to have a 4 cm radius with 10,000 Amp-turn current in each coil. The two lens combinations in Figure 1 are shown in the table below with the resulting angular frequencies.

For a range of values of  $\tau_1$ , and  $\tau_2$ , we then solve the radial and axial simultaneous equations (8) (i.e.  $\mathcal{B}_r = 0$ ,  $\mathcal{B}_z = 0$ ) to determine  $t_1$  and  $t_2$ . Although both  $\mathcal{B}_z$  and  $\mathcal{B}_r$  are quadratic in  $t_1$  and  $t_2$ , substitution for either of these variables leads to a final

Strategy	1st lens	$\omega_{1r}$	$S_1$	2nd lens	$\omega_{2r}$	$S_2$	$\xi$
AR	Axial focus	58i rad s <sup>-1</sup>	2.63	Radial focus	97 rad s <sup>-1</sup>	0.58	> 1
RA	Radial focus	97 rad s <sup>-1</sup>	0.58	Axial focus	58i rad s <sup>-1</sup>	2.63	< 1

**Table 1.** The two different alternate-gradient strategies modelled. The  $\omega$ 's are the lens strengths,  $S$ 's are the coil separations and  $\xi = \sigma_z/\sigma_r$  is the cloud aspect ratio.

sixth polynomial equation. This must therefore be solved numerically and leads to six solution pairs  $(t_1, t_2)$ . Only solution pairs with real times  $0 \leq t_1, t_2 \leq T$  satisfying the condition  $t_1 + \tau_1 + t_2 + \tau_2 \leq T$  are considered. The number of  $(t_1, t_2)$  solution pairs as a function of  $\tau_1$  and  $\tau_2$  is shown in Figure 3(a). These  $(t_1, t_2)$  solution pairs can then be used to calculate the relative increase in atomic density of a cold atom cloud. From equation (6) the relative density increase of the image is thus:

$$\rho_{3D} = \frac{\sigma_R^3}{((\mathcal{A}_r\sigma_R)^2 + (\mathcal{B}_r\sigma_V)^2)\sqrt{(\mathcal{A}_z\sigma_R)^2 + (\mathcal{B}_z\sigma_V)^2}} \rightarrow \frac{1}{\mathcal{A}_r^2\mathcal{A}_z}. \quad (9)$$

Where the arrow indicates the limit  $\mathcal{B} = 0$ . The dimensionless relative density increases obtained for both strategies are shown in Figure 3(b,c). These plots are then effectively combined in Figure 3(d) by inverting  $\tau_1, \tau_2$  to find the relative density increase as a function of the parameters  $\lambda_1, \lambda_2$  which are the mean relative times of the radially diverging and converging lens.

#### 4. A measure of the quality of the focus

The attributes of parabolic lenses are unimportant, unless it can be shown that experimentally realistic lenses are sufficiently parabolic for such an approximation to be appropriate. At the end of [13] there appeared to be a major difference between the parabolic approximation and real lenses. To some extent, this may have been due to the way the lens properties were measured.

In [13] numerical integration of the forces arising from the magnetic fields due to current loops (generated by the Biot-Savart law) was used, to track the trajectories of several ( $\approx 1000$ ) simulated atoms. The initial positions and velocities of the atoms were randomly assigned, weighted according to isotropic Gaussian spatial and velocity distributions with 1D standard deviations of  $\sigma_R = 0.4$  mm and  $\sigma_V = 4.4$  cm/s (as discussed in the previous section). The way in which the harmonicity of a lens was measured was to compare the expected harmonic focus size to the rms radii of the simulated atom cloud at the time of the harmonic focus. The important drawback of this rms approach is that the final location of atoms after a magnetic lens is highly nonlinear with respect to initial conditions. An atom with a velocity in the wings of the initial Gaussian distribution will experience highly anharmonic lensing, as it will be far from the centre of the lens during the magnetic impulse. Thus a few atoms can completely alter the rms width of the cloud.

Another method to quantify the focus, adopted here, is to monitor the fraction of the atoms entering the focus region of a purely harmonic lens. The initial radial and axial cloud standard deviations are  $\sigma_R$ , so the final standard deviations for a harmonic lens are  $\sigma_r = \mathcal{A}_r\sigma_R$  and  $\sigma_z = \mathcal{A}_z\sigma_R$ . By renormalising the dimensions

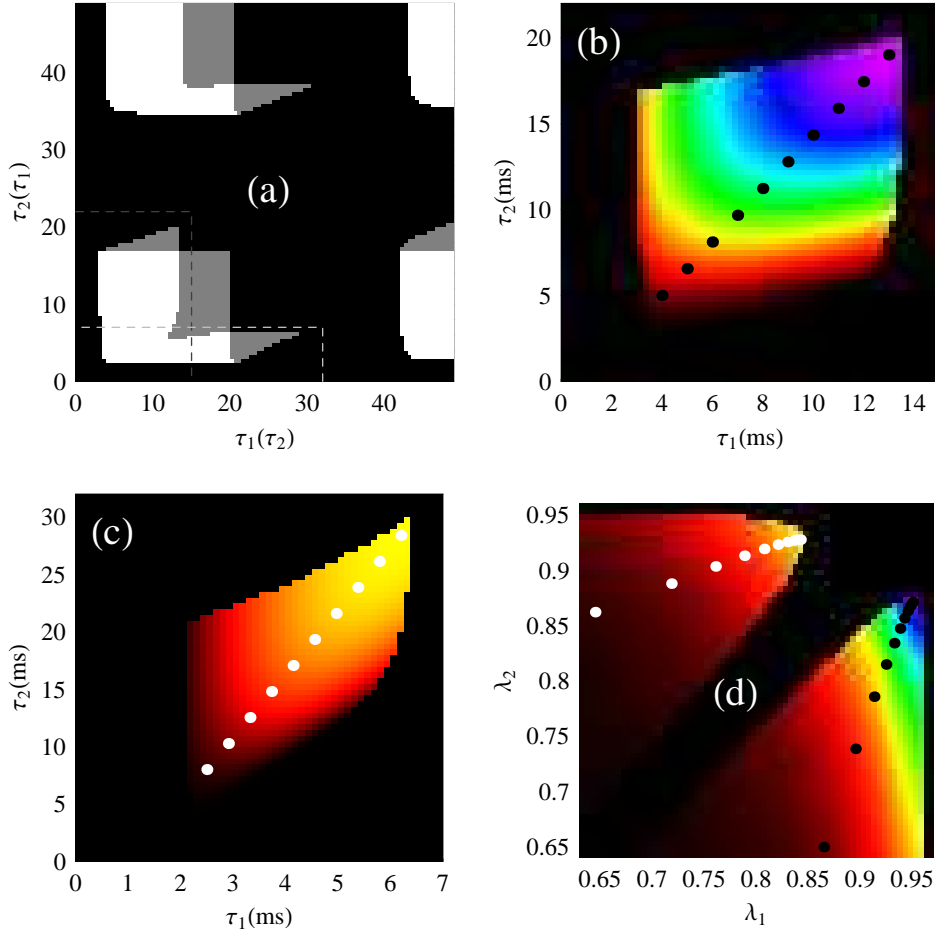


**Figure 3.** Image (a) shows the number of solution pairs (black=0, grey=1, white=2) for  $(t_1, t_2)$  as a function of  $\tau_1$  and  $\tau_2$  ( $\tau_2$  and  $\tau_1$ ) in ms for Strategy AR (Strategy RA). The two dashed regions of the ‘solution island’ lead to the highest relative density increases, shown in (b) and (c). The relative density increase (equation (9)) if one images a cloud of atoms using: (b) Strategy AR, (c) Strategy RA. The maximum relative density increases are 1100 (320), for a  $\xi = 17$  sausage ( $\xi = 0.094$  pancake) shaped cloud, for images (b) and (c) respectively. The results of (b) and (c) are combined in (d), the relative density increase in terms of  $\lambda_1$  and  $\lambda_2$  (the mean times of the radially converging and radially diverging impulses relative to  $T$ ). The points in images (b)-(d) are used later as a sample in simulations.

so that the radial and axial dimensions are measured in terms of these final focus standard deviations, then a sphere with radius  $R_0 = 1.53817$  defined by

$$\frac{\int_0^{R_0} r^2 e^{-\frac{r^2}{2}} dr}{\int_0^\infty r^2 e^{-\frac{r^2}{2}} dr} = \frac{1}{2} \quad (10)$$

will contain half of the atoms of the focused Gaussian distribution. For numerical

simulations the fraction of atoms entering this harmonic focus is measured, and multiplied by twice the relative density increase of a purely harmonic lens (i.e.  $2\mathcal{A}_r^{-2}\mathcal{A}_z^{-1}$ ) to get a measure of the relative density increase afforded by a real lens.

Note that the centre of the harmonic focus region, as well as the centre about which the rms radius is defined, is the final position of an atom initially in the centre of the Gaussian position and velocity distributions. This will lead to a slight underestimation in the density increase regardless of which way it is defined (it has been assumed the mean cloud position follows the initial centre-of-mass). In addition the density can increase if the best experimental 3D focus occurs at a time other than the best parabolic lens focus time, but the focus time has been allowed to vary in the simulations. For more details on the effects of gravity on launched atoms, namely that even the centre-of-mass atoms will experience time-varying radial and axial harmonic trap frequencies, see the Appendix.

#### 4.1. Single-impulse focusing revisited

In light of the above discussion, 3D single-impulse focusing outlined in [13] is briefly revisited, in particular Strategy VI: the baseball coil system. This system consisted of a square baseball coil with side lengths  $w$  and a coil pair of radius  $w$  separated by  $w$  that were coaxial with the baseball coil axis. The current in the baseball coil was 10,000 Amp-turns, and an isotropic lens is formed when the coil pair has a current of 1,541 Amp-turns. In this paper we have made the value  $w = 4$  cm, leading to an angular frequency  $\omega = 62$  rad/s in the harmonic lens. This is to provide a better comparison between single- and double-impulse techniques.

In Figure 4 the relative density increase after the baseball lens is plotted in terms of the parameter  $\lambda$  (the effective time of the baseball lens relative to  $T$ ). The red dots correspond to the relative density increase using rms widths for the volume. The blue dots show the relative density increase as the fraction of atoms in the harmonic focus zone times the harmonic density increase. It is clear that we reach very different conclusions based on whether the rms radius of the focused atomic cloud, or the fraction of atoms which reach the harmonic focus are considered.

By only looking at rms widths the optimum lens position occurs at  $\lambda = 0.3$ , corresponding to a factor of 50 decrease in density. However considering the fraction of atoms in the harmonic focus zone times the harmonic density increase, the optimum position is now  $\lambda = 0.9$ . The relative density increase is 2.3, which corresponds to 0.3% of the cloud focused to a density 729 times greater than it was originally.

The source of this discrepancy between methods can be seen in Figure 4 (b-c) where the non-Gaussian wings produce an over estimate of the rms cloud width. The  $y$  and  $z$  standard deviations for the Gaussian fits (black curves) are  $730 \mu\text{m}$  and  $820 \mu\text{m}$  respectively; an almost isotropic distribution.

#### 4.2. Alternate gradient

This section compares the alternate gradient numerical simulations with the purely harmonic lenses of section 3. The  $(\tau_1, \tau_2)$  sample co-ordinates illustrated in Figure 3(b-c) are used, in order to run numerical simulations for the relative density increases illustrated in Figure 5. We have not (cf. Figure 4) used the rms volume of the cloud to show the relative density increases as these result in extremely low relative density



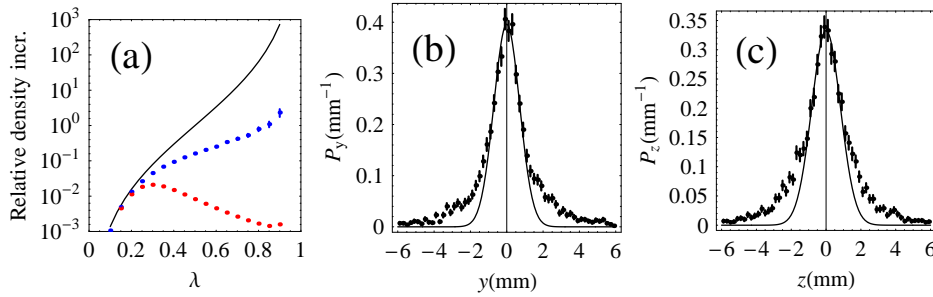


**Figure 4.** Image (a) shows the relative density increase (with error bars, for a 5000 atom simulation) based on: a purely harmonic lens (black curve), the fraction of atoms in a real lens arriving at the harmonic focus region (blue dots), the ratio of rms cloud volume before and after a real lens (red dots). Images (b) and (c) show the spatial probability distributions at the focus (black dots) in the  $y$  and  $z$  directions, respectively, where the non-Gaussian wings of the distribution can be clearly seen. These two distributions are taken from the  $\lambda = 0.5$  lens simulation, in which case 16% of the atoms are in the harmonic focus region. The Gaussian fits in (b) and (c) (as well as the  $x$  distribution) have an area of  $\approx 70\%$ .

increases (typically  $10^{-5}$  in (a) and  $10^{-3}$  in (b)) that would reduce the contrast in Figure 5.

For both strategies the numerical simulations trace the shape of the analytical relative density increase although aberrations result in reduced increases. The maximum relative density increases in (a) and (b) are 186 and 50 respectively. This is a marked improvement on the single-impulse focusing, however the cloud distribution is no longer isotropic. The harmonic focus aspect ratio has a range  $12 \leq \xi \leq 17$  in (a) and  $0.074 \leq \xi \leq 0.095$  in (b).

In certain applications, for example microtrap loading and lithography, the sausage-shaped distribution with its reduced radial spread could be beneficial. Figure 5 (c) plots the distribution of a cloud focused via Strategy AR. The standard deviations for the Gaussian fits to the core of the  $x$ ,  $y$ , and  $z$  distributions are  $56 \mu\text{m}$ ,  $56 \mu\text{m}$  and  $850 \mu\text{m}$ ; an order of magnitude reduction in the radial direction compared with single-impulse focusing.

Given comparable lens dimensions and strengths, double-impulse magnetic focusing is far superior to single-impulse magnetic focusing in terms of the relative density increases that can be achieved by a fraction of the atoms. This result is in stark contrast to the relative rms density increase of the entire cloud, which would lead to the opposite conclusion. This spatial focusing would find applications in lithography or sending the atomic cloud through micro-sized apertures.

## 5. Physical properties of clouds focused via the alternate gradient method

For many experiments it is also important to consider changes to the velocity distribution and hence the collision rate and phase-space density. Unless the collision rate of a gas is sufficiently high, then Bose-Einstein condensation via sustainable evaporative cooling is impossible. Changes in the collision rate and phase-space density of the focused cloud are complicated by the fact that alternate-gradient lensing

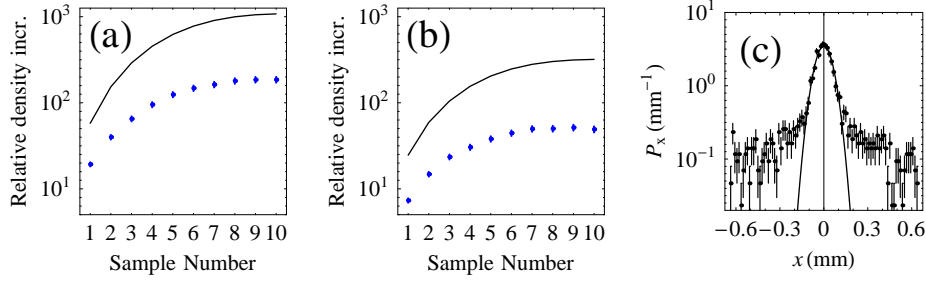


**Figure 5.** Images (a) and (b) use the  $(\tau_1, \tau_2)$  co-ordinates illustrated in Figure 3(b) and (c) to show the relative density increase for alternate gradient lensing Strategies AR and RA, respectively. There were 1000 atoms in the simulation and relative density increases are shown for a pure harmonic lens (black curve), as well as the relative density increase for the fraction of atoms in a real lens arriving at the harmonic focus region (blue dots with error bars). In image (c) the strong spatial bimodal nature of the  $x$  focus for the leftmost point in (a) is clearly seen on a log scale. The Gaussian fit (with  $\sigma_x = 56 \mu\text{m}$ ) contains 49% of the 3000 simulated atoms used in (c).

automatically leads to an anisotropic focused distribution both in space *and* in velocity.

At the  $\mathcal{B}_{r,z} = 0$  focus of the cloud the  $\mathcal{ABCD}_{r,z}$  matrix has radial and axial spatial widths  $\sigma_r = \langle r^2 \rangle^{1/2} = \mathcal{A}_r \sigma_R$  and  $\sigma_z = \langle z^2 \rangle^{1/2} = \mathcal{A}_z \sigma_R$  respectively. The radial and axial velocity widths are given by:

$$\sqrt{\langle v_{r,z}^2 \rangle} = \sqrt{k_B \mathcal{T}_{r,z} / m} = \sqrt{\mathcal{C}_{r,z}^2 \sigma_R^2 + \sigma_V^2 / \mathcal{A}_{r,z}^2}, \quad (11)$$

where  $\mathcal{T}_{r,z}$  is the atomic cloud temperature. In the limit  $\mathcal{C}_{r,z} \sigma_R \ll \sigma_V / \mathcal{A}_{r,z}$  (which is not always the case), the velocity width of the focused cloud is inversely proportional to its spatial width and  $\sqrt{\langle v_{r,z}^2 \rangle} = \sigma_V / \mathcal{A}_{r,z}$ . In Figure 6 phase-space plots of the AR and RA strategies from the rightmost points of Figures 5 (a) and (b) were generated with a 30,000 atom simulation. The effect of aberration is clearly seen when comparing the purely harmonic lenses (subscript H) and the Monte Carlo simulation with the full magnetic fields from realistic coils (subscript MC). The plots also demonstrate the inversely proportional relationship between spatial and velocity widths. Furthermore, in the Monte Carlo simulations there is much stronger correlation between position and velocity.

The anisotropic temperature in the focused cloud means that captured atoms in a cylindrically symmetric harmonic trap with radial and axial frequencies  $\nu_r$  and  $\nu_z$ , will rethermalise to an isotropic temperature via elastic collisions. The total (potential+kinetic) energy of the focused cloud is equated with that of a 3D harmonic oscillator at equilibrium temperature  $\mathcal{T}$  (i.e.  $\frac{1}{2} k_B \mathcal{T}$  average energy per atom for each space and velocity dimension). The equilibrium temperature of the focused cloud after thermalisation is thus:

$$\mathcal{T} = \frac{m}{6k_B} (4\pi^2 (2\nu_r^2 \langle r^2 \rangle + \nu_z^2 \langle z^2 \rangle) + (2\langle v_r^2 \rangle + \langle v_z^2 \rangle)). \quad (12)$$

In many experiments other physical properties of the atomic cloud are of interest: the atomic density  $n \propto 1/(\sigma_r^2 \sigma_z)$ , collision rate  $\gamma \propto n \sqrt{\mathcal{T}}$  and phase-space density PSD  $\propto n/(\mathcal{T}_r \mathcal{T}_z^{1/2})$ . In order to minimise the loss of phase-space density during

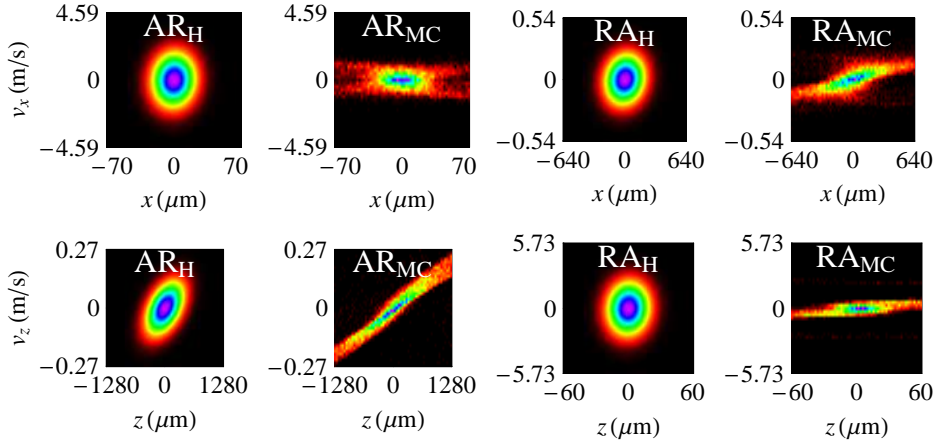


**Figure 6.** Phase-space plots of the AR and RA strategies from the rightmost points of Figures 5 (a) and (b) respectively. Both a harmonic lens calculation (subscript  $H$ ) and a Monte Carlo simulation with the full magnetic fields from realistic coils (subscript MC) are plotted. In the  $AR_{MC}$  plot there are 45% ( $x-v_x$ ) and 42% ( $z-v_z$ ) of the initial 30,000 atoms present. In the  $RA_{MC}$  plot there are 61% ( $x-v_x$ ) and 24% ( $z-v_z$ ) of the atoms present. The effects of aberration are clearly seen when comparing the harmonic and realistic magnetic coils.

thermalisation of the focused cloud, one can show that it is best to choose  $\nu_r$  and  $\nu_z$  such that the potential energy is equal in all spatial dimensions and the total potential energy is equal to the total kinetic energy of the cloud.

The physical properties of the focused atomic clouds of Figure 6 are displayed in Table 2. The relative values for the density  $n$ , collision rate  $\gamma$  and phase-space density can be converted into absolute values using typical initial experimental values  $\langle n \rangle = 10^{10} \text{ cm}^{-3}$  (an atom number  $N = 3 \times 10^7$  in the unfocused cloud),  $\gamma = 1 \text{ Hz}$  (for  $^{87}\text{Rb}$  with the low-temperature collision cross-section  $\sigma = 8\pi a^2 = 8 \times 10^{-12} \text{ cm}^2$ ) and phase-space density  $\text{PSD} = 2 \times 10^{-6}$ . Aberrations will effectively be smaller if a large MOT is used with the same density (e.g.  $N = 10^9$ ,  $\sigma_R = 1.3 \text{ mm}$ ) and temperature as Table 2, and a trap with weaker frequencies to catch the atoms.

Note that the Monte Carlo relative density increases in Table 2 are lower than those in Figure 5 by a factor of  $\approx 2$ , but the fraction of atoms in the focus are higher by a factor of  $\approx 2$ . In Figure 5 the density is estimated by measuring the fraction of atoms arriving at the harmonic focus. Here, a 6-dimensional Gaussian phase-space fit to the narrow central peak of the bimodal focus was made to explicitly obtain  $\sigma_r$ ,  $\sigma_z$ ,  $\mathcal{T}_r$  and  $\mathcal{T}_z$ . The fraction of atoms in this Gaussian focus was used for  $P$  here.

An interesting result of Table 2 is that the aberrations of ‘real’ lenses work to our advantage, to some extent, in that the atoms can be loaded into a trap with a shallower depth than atoms focused by a purely harmonic lens, and phase-space density loss is reduced during rethermalisation. This is due to the reduced anisotropy of the spatial and velocity distributions at the focus. The focused atoms have a relatively high temperature and one needs a trap depth of  $\approx 10 \text{ mK}$  to trap the focused atoms. For an atom with a magnetic moment of one Bohr magneton  $\mu_B$ , this corresponds to a

	t	$P$	$\sigma_{r,z}(\mu\text{m})$	$\mathcal{T}_{r,z}(\mu\text{K})$	$\nu_{r,z}(\text{Hz})$	$n$	$\gamma$	PSD
AR <sub>H</sub>	0	1	400, 400	20, 20	<i>17.4, 17.4</i>	1	1	1
	$T$	1	15.2, 257	13900, 60.9	<i>12000, 47.3</i>	1080	23200	0.892
	$T_R$	1	15.2, 257	9260, 9260	9850, 584	1080	23200	0.108
AR <sub>MC</sub>	0	1.000	400, 400	20, 20	<i>17.4, 17.4</i>	1	1	1
	$T$	0.308	23, 500	2720, 57	<i>3530, 23.5</i>	74.5	713	0.325
	$T_R$	0.308	23, 500	1830, 1830	2900, 133	74.5	713	0.085
RA <sub>H</sub>	0	1	400, 400	20, 20	<i>17.4, 17.4</i>	1	1	1
	$T$	1	128, 12.2	197, 21600	<i>170, 18700</i>	319	6110	0.988
	$T_R$	1	128, 12.2	7320, 7320	1040, 10900	319	6110	0.046
RA <sub>MC</sub>	0	1.000	400, 400	20, 20	<i>17.4, 17.4</i>	1	1	1
	$T$	0.305	200, 20	105, 1670	<i>79.7, 3180</i>	24.4	137	0.509
	$T_R$	0.305	200, 20	627, 627	195, 1950	24.4	137	0.139

**Table 2.** Physical properties of the two different alternate-gradient strategies modelled, AR and RA from the rightmost points in Figs. 5 (a) and (b) respectively. Subscripts H and MC respectively denote a simulation with purely harmonic lenses and a Monte Carlo simulation with the full magnetic fields from realistic lens coils. The measured parameters are: fraction of atoms in the Gaussian focus  $P$  (see text), radial/axial cloud radius  $\sigma_{r,z}$ , radial/axial temperature  $\mathcal{T}_{r,z}$ , radial/axial trap frequency  $\nu_{r,z}$ , relative density  $n$ , relative collision rate  $\gamma$  and relative phase space density PSD. The effective trap frequencies for the initial ( $t = 0$ ) and focused ( $t = T$ ) cloud (italicised) are equilibrium values based on  $\nu = \frac{1}{2\pi\sigma} \sqrt{k_B T/m}$ . The actual frequencies of the trap the atoms are loaded into at  $t = T$  are denoted in the  $t = T_R$  lines (the cloud properties after  $T$  plus the thermalisation time).

magnetic trap depth 150 G.

## 6. Discussion and conclusion

The main application of interest for the magnetically imaged atoms will be loading a magnetic microtrap or optical dipole trap, for which alternate gradient imaging is well-suited. If the trap that is being loaded is harmonic, with a large capture volume, then the rms size of the cloud will be linked to the equilibrium temperature after elastic collisions rethermalise the initially bimodal image distribution. In order to keep the high density core of the atomic cloud, the high energy atoms must be removed on a time scale that is rapid compared to rethermalisation - this could be achieved with strong RF evaporative cooling or by shining resonant dark SPOT beams [22] at the focal region. A trap with a small capture volume, e.g. an atom chip [16] or a focused optical dipole beam trap [17], is ideal as only the high density core of atoms will be captured in the trap.

The timescale needed to remove the shell of hot diffuse atoms from the central core will actually be much longer than the time it takes for the dense core atoms (which are anisotropically focused in space and velocity) to thermalise to a uniform temperature in 3D. The higher the anisotropy of the focused atomic cloud, the more phase space density is lost during the thermalisation. This loss could be mitigated to some extent if the radial and axial trap frequencies were varied to remain in equilibrium with the changing radial and axial cloud temperatures during the (short) thermalisation time.

In this paper we have used experimentally realistic parameters to compare the limiting focal size of a launched cold cloud of weak-field seeking atoms subject to

either a single or double magnetic lens impulse. The  $ABCD$  matrix formalism was convenient for giving an estimate as to the parameters needed for magnetic focusing, but numerical simulations were necessary to detect the effects of aberrations in real magnetic lenses. If one wishes to minimise the rms image volume of a launched cloud then a single-impulse lens is preferable. If, however, one can selectively capture the central core of the bi-modal image, a double-impulse (alternate gradient) lens can lead to orders of magnitude relative density increases for both pancake- and sausage-shaped image clouds. Although we have only considered cold thermal atomic clouds in this paper, the effects of aberrations will also be important for tight focusing of coherent matter waves [6, 23].

### Acknowledgments

This work is supported by EPSRC, the UKCAN network and Durham University. We thank Charles Adams, Simon Gardiner and Kevin Weatherill for fruitful discussions.

### Appendix: modelling time varying lens strengths

This paper has only discussed parabolic lenses with constant strength  $\omega$ , pulsed on with a top-hat pulse of duration  $\tau$ . In experiments the lens strength is a function of time, partly because the current in a real coil is not a top-hat pulse, and partly because the centre-of-mass of a launched atomic cloud changes as it goes through a lens and thus (to second order in position) will experience a time-varying parabolic lens. In practice it was unnecessary to adjust the timing or lens coil positions to allow for these effects in the simulations, however we briefly discuss ways around this issue should it become problematic.

A harmonic lens with arbitrary time variation  $\omega(t)$  (where  $\omega(t)$  and its derivatives are zero outside the experimental pulse time  $t_1 \leq t \leq t_1 + \tau_1$ ), is equivalent to an infinite product of infinitesimal  $2 \times 2$  translation and thin lens matrices, resulting in a single  $2 \times 2$  matrix that is itself independent of the initial velocity and position of an atom. On solving  $y''[t] = -\omega^2[t]y[t]$  from  $t = t_1$  to  $t = t_1 + \tau_1$ , with the initial conditions  $\{y[t_1], y'[t_1]\} = \{dy, 0\}$  to get  $\{y[t_1 + \tau_1], y'[t_1 + \tau_1]\} = \{\mathcal{A}, \mathcal{C}\}dy$ , then use initial conditions  $\{y[t_1], y'[t_1]\} = \{0, dv\}$  to get  $\{y[t_1 + \tau_1], y'[t_1 + \tau_1]\} = \{\mathcal{B}, \mathcal{D}\}dv$ , (with small values for  $dy$  and  $dv$ ) results in the general  $ABCD$  matrix for any initial position and velocity from (numerically or analytically) solving the differential equation for only two different initial conditions. As this  $ABCD$  matrix has determinant 1 (it is a product of determinant 1 matrices) it can be expressed as a (translation matrix)-(thin lens)-(translation matrix) combination.

One can then use an iterative 4D Newton-Raphson method with four input parameters (the  $z$  positions of the two alternate gradient lenses and the times  $t_1$  and  $t_2$ ) such that the  $z$  centre-of-mass velocity of the atoms is not altered by either lens, and  $\mathcal{B}_r$  and  $\mathcal{B}_z$  are identical to zero.

### References

- [1] Adams C S, Sigel M and Mlynek J 1994 *Phys. Rep.* **240** 143
- [2] Adams C S and Riis E 1997 *Prog. Quant. Elec.* **21** 1
- [3] Chu S 1998 *Rev. Mod. Phys.* **70** 685; Cohen-Tannoudji C N 1998 *Rev. Mod. Phys.* **70** 707; Phillips W D 1998 *Rev. Mod. Phys.* **70** 721
- [4] Hinds E A and Hughes I G 1999 *J. Phys. D* **32** R119

- [5] Roach T M, Abele H, Boshier M G, Grossman H L, Zetie K P and Hinds E A 1995 *Phys. Rev. Lett.* **75** 629; Sidorov A I, McLean R J, Rowlands W J, Lau D C, Murphy J E, Walciewicz M, Opat G I and Hannafor P 1996 *Quantum Semiclass. Opt.* **8** 713; Lau D C, Sidorov A I, Opat G I, McLean R J, Rowlands W J and Hannafor P 1999 *Eur. Phys. J. D* **5** 193; Lev B, Lassailly Y, Lee C, Scherer A, Mabuchi H 2003 *Applied Physics Letters* **83** 395; Hughes I G *et al.* 1997 *J. Phys. B: At. Mol. Opt. Phys.* **30** 647; *ibid* **30** 2119; *ibid* **34** 2869; Saba C V *et al.* 1999 *Phys. Rev. Lett.* **82** 468; Rosenbusch P *et al.* 2000 *Phys. Rev. A* **61** 031404; Rosenbusch P *et al.* 2000 *Appl. Phys. B* **70** 709; Kadio D, Houde O and Pruvost L 2001 *Europhys. Lett.* **54** 417
- [6] Bloch I, Köhl M, Greiner M, Hänsch T W and Esslinger T 2001 *Phys. Rev. Lett.* **87** 030401; Arnold A S, MacCormick C and Boshier M G 2002 *Phys. Rev. A* **65** 031601(R); Arnold A S, MacCormick C and Boshier M G 2004 *J. Phys. B* **37** 485
- [7] Meschede D and Metcalf H 2003 *J. Phys. D* **36** R17
- [8] Szymaniec K, Davies H J and Adams C S 1999 *Europhysics Letters* **45** 450
- [9] Salomon Ch *et al.* 2001 C. R. Acad. Sci. Paris. Serie IV, 1313
- [10] Cornell E A, Monroe C and Wieman C E 1991 *Phys. Rev. Lett.* **67** 2439
- [11] Maréchal E, Guibal S, Bossennec J L, Gorza M P, Barbé R, Keller J C and Gorceix O 1998 *Eur. Phys. J. D* **2** 195; Maréchal E, Guibal S, Bossennec J L, Barbe R, Keller J C and Gorceix O 1999 *Phys. Rev. A* **59** 4636
- [12] Miossec T, Barbé R, Keller J-C and Gorceix O 2002 *Opt. Commun.* **209** 349
- [13] Pritchard M J, Arnold A S, Smith D A and Hughes I G 2004 *J. Phys. B* **37** 4435
- [14] Smith D A, Pritchard M J, Arnold A S and Hughes I G *In preparation.*
- [15] Müller D, Anderson D Z, Grow R J, Schwindt P D D and Cornell E A 1999 *Phys. Rev. Lett.* **83** 5194; Dekker N H, Lee C S, Lorent V, Thywissen J H, Smith S P, Drndić M, Westervelt R M and Prentiss M 2000 *Phys. Rev. Lett.* **84** 1124; Key M, Hughes I G, Rooijackers W, Sauer B E, Hinds E A, Richardson D J and Kazansky P G 2000 *Phys. Rev. Lett.* **84** 1371
- [16] Folman R, Kruger P, Schmiedmayer J, Denschlag J and Henkel C 2002 *Adv. At. Mol. Opt. Phys.* **48** 263; Reichel J 2002 *Applied Physics B* **74** 469
- [17] Grimm R, Weidemuller M and Ovchinnikov Y 1999 *Adv. At. Mol. Opt. Phys.* **42** 95
- [18] Petrich W, Anderson M H, Ensher J R and Cornell E A 1995 *Phys. Rev. Lett.* **74** 3352
- [19] Earnshaw S 1842 *Trans. Cambridge Philos. Soc.* **7** 97; Wing W H 1984 *Prog. Quant. Electr.* **8** 181
- [20] Lawson J D 1977 *The Physics of Charged Particle Beams* (OUP, Oxford)
- [21] Bethlem H L and Meijer G 2003 *Int. Rev. Phys. Chem.* **22** 73; Tarbutt M R, Bethlem H L, Hudson J J, Ryabov V L, Ryzhov V A, Sauer B E, Meijer G and Hinds E A 2004 *Phys. Rev. Lett.* **92** 173002
- [22] Ketterle W, Davis K B, Joffe M A, Martin A and Pritchard D E 1993 *Phys. Rev. Lett.* **70** 2253
- [23] Murray D R and Öhberg P 2005 *J. Phys. B* **38** 1227